SKYEVENTS: A LARGE-SCALE EVENT-ENHANCED UAV DATASET FOR ROBUST 3D SCENE RECONSTRUCTION

Anonymous authors
Paper under double-blind review

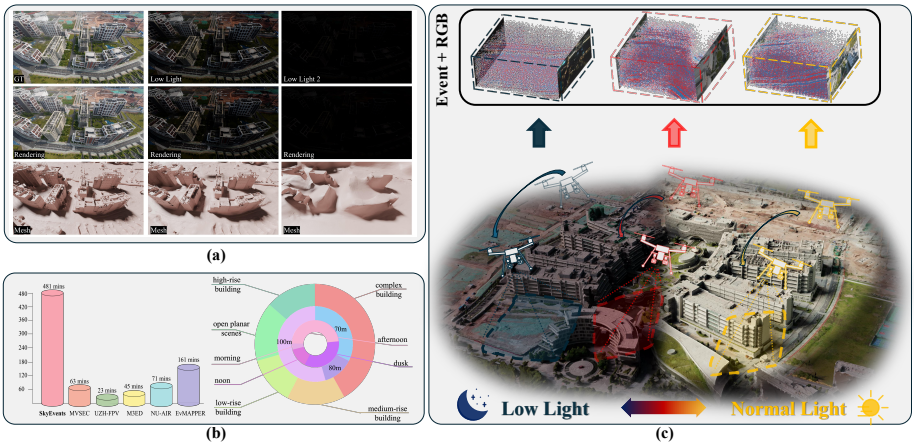

Figure 1: (a) Rendering and mesh under different light conditions. (b) Comparison and statistics of datasets. (c) Dataset collection across varied illumination conditions, scenarios, and flight altitudes.

ABSTRACT

Recent advances in large-scale 3D scene reconstruction using unmanned aerial vehicles (UAVs) have spurred increasing interest in neural rendering techniques. However, existing approaches with conventional cameras struggle to capture consistent multi-view images of scenes, particularly in extremely blurred and low-light environments, due to the inherent limitations in dynamic range caused by long exposure and motion blur resulting from camera motion. As a promising solution, bio-inspired event cameras exhibit robustness in extreme scenarios, thanks to their high dynamic range and microsecond-level temporal resolution. Nevertheless, dedicated event datasets specifically tailored for large-scale UAV 3D scene reconstruction remain limited. To bridge this gap, we introduce **SkyEvents**, a pioneering large-scale event-enhanced UAV dataset for 3D scene reconstruction, incorporating RGB, event, and LiDAR data. SkyEvents encompasses 45 sequences, spanning over 8 hours of video, captured across a diverse set of illumination conditions, scenarios, and flight altitudes. To facilitate the event-based 3D scene reconstruction with SkyEvents, we propose the Geometry-constrained Timestamp Alignment (**GTA**) module to align timestamps between the event and RGB cameras. Furthermore, we introduce Region-wise Event Rendering (**RER**) loss for supervising the rendering optimization. With SkyEvents, we aim to motivate and equip researchers to advance large-scale 3D scene reconstruction in challenging environments, harnessing the unique strengths of event cameras.

1 INTRODUCTION

Large-scale 3D scene acquisition using unmanned aerial vehicles (UAVs) has become a central tool for urban modeling, digital twins, and robotics applications. Driven by the growing demand for accurate and detailed reconstructions of city-scale environments, neural rendering techniques, such as Neural Radiance Fields (NeRF) (Mildenhall et al., 2021) and 3D Gaussian Splatting (3DGS) (Kerbl et al., 2023), have been extended from small object-centric captures (Barron et al., 2022; Müller et al., 2022; Li et al., 2023; Huang et al., 2024; Yu et al., 2024; Guédon & Lepetit, 2023) to large-scale scenes (Tancik et al., 2022; Turki et al., 2022; Mi & Xu, 2023; Lin et al., 2024; Yu Chen, 2024; Liu et al., 2025; Li et al., 2025). However, existing approaches still fundamentally rely on conventional CMOS-based RGB cameras, which remain highly susceptible to the limitations in challenging conditions-especially in scenarios with motion blur and insufficient illumination (Cladera et al., 2025). This inherent limitation often leads to a degradation in the quality of 3D reconstructions under low-light and motion-blurred conditions (Zahid et al., 2025; Matta et al., 2025; Zhang et al., 2025), thus limiting the achievable reconstruction fidelity (see Figure 1(a)).

To address this, event cameras have emerged as a promising alternative visual sensing paradigm, providing a complementary modality for 3D reconstruction. Unlike conventional cameras, event-based sensors asynchronously record changes in scene brightness at microsecond resolution, offering significantly improved temporal fidelity, a wide dynamic range, and robustness to motion blur (Xu et al., 2025). These advantages have made event cameras increasingly popular in 3D reconstruction, where they have been successfully combined with NeRF and 3DGS techniques to enhance the robustness of reconstructions in dynamic and low-light environments (Yura et al., 2025; Zhang et al., 2025; Zhu et al., 2024; Low & Lee, 2023).

Despite the growing efforts in event cameras for 3D reconstruction, a key limitation remains: *the lack of suitable, event-enhanced UAV datasets tailored for large-scale 3D scene reconstruction*. While recent event-enhanced UAV datasets have laid important groundwork, they often lack the necessary modalities and ground truth required for high-fidelity city-scale 3D reconstruction (in Table 1). For instance, datasets such as MVSEC (Zhu et al., 2018) and UZH-FPV (Delmerico et al., 2019) include aerial sequences, but they lack synchronized high-resolution RGB frames or volumetric ground truth, limiting their utility for neural rendering. Similarly, M3ED (Chaney et al., 2023) and NU-AIR (Iaboni et al., 2025) offer useful event streams and RGB imagery but do not provide the dense depth and 6-DoF pose supervision necessary for large-scale 3D reconstruction. The most recent work, EvMAPPER (Cladera et al., 2025), pioneers event-based orthomapping for high-altitude flights, but its focus on planar mosaics does not address the challenges of trajectory complexity and frame jitter that are inherent to low-altitude, large-scale 3D modeling.

To address it, we introduce *SkyEvents*, the first dataset specifically designed for event-enhanced UAV 3D reconstruction. SkyEvents brings together challenging low-light and motion-blurred conditions, synchronized RGB frames, dense per-frame depth supervision, high-quality 3D ground-truth reconstructions, and accurate 6-DoF UAV poses within a benchmark dataset. The data is collected using a DJI Matrice 350 equipped with a centimeter-accurate real-time kinematics system, flying over five distinct areas at altitudes ranging from 70 to 100 meters (see Figure 1(c)). DJI L2 LiDAR data serves as the ground truth due to its illumination-invariant nature and high precision. In total, the dataset contains 45 sequences (spanning over 8 hours) of paired RGB and event data, along with 0.72 km^2 of point cloud data capturing at 2.64 cm/pixel GSD, enabling the robust development of perception algorithms under real-world conditions (see Figure 1(b)).

To enable event-based 3D reconstruction with SkyEvents, we introduce two key components: the Geometry-Constrained Timestamp Alignment (**GTA**) module, which aligns event and RGB data based on temporal constraints, and the Region-Wise Event Rendering (**RER**) loss, which optimizes event-based rendering. We evaluate the effectiveness of the proposed GTA and RER modules with existing neural rendering techniques using the SkyEvents dataset. Our experiments demonstrate the potential of event data for 3D scene reconstruction, particularly in challenging environments.

Dataset	Low-light/night	RGB	RGB Rate	RGB FoV	Event FoV	Depth	Geometry GT	6-Dof Pose	Resolution	Duration[1]
MVSEC (Hexacopter) (Zhu et al., 2018)	✓[2]	✗	✗	✗	83°	✓	✗	✓	346×260	63
UZH-FPV (Delmerico et al., 2019)	✗	✓	30/50 Hz	186°	120°	✗	✗	✓	346 × 260	23
M3ED (UAV splits) (Chaney et al., 2023)	✗	✓	30 Hz	52°	63°	✓	✗	✓	1280×720	45
NU-AIR (Iaboni et al., 2025)	✗[3]	✗	✗	✗	70°	✗	✗	✗	640×480	71
EvMAPPER (Cladera et al., 2025)	✓	✓	50 Hz	71°	64°	✗	✗	✗	1280×720	161
SkyEvents	✓	✓	120 Hz	71°	45°	✓	✓	✓	1280×720	**481**

[1] In minutes, [2] dusk-only, [3] multiple illumination conditions.

Table 1: Comparison of SkyEvents with previous event-based UAV datasets.

Contributions. (1) We present *SkyEvents*, a first large-scale event-enhanced UAV dataset for 3D scene reconstruction, including synchronized RGB and event data, LiDAR data, and accurate 6-DoF UAV poses. (2) We introduce two key components for integrating event modality into neural rendering-based 3D reconstruction: Geometry-constrained Timestamp Alignment (GTA) module and Region-wise Event Rendering (RER) loss. (3) Experiments demonstrate that event-guided neural rendering outperforms RGB-only baselines, achieving higher texture fidelity and geometric accuracy in large-scale 3D reconstructions under low-light and motion-blurred environments.

2 Related Works

2.1 3D Scene Reconstruction

3D scene reconstruction seeks to recover the geometric structure of a scene from multi-view images or other modality data. Neural Radiance Fields (NeRF) (Deng et al., 2022; Garbin et al., 2021; Mildenhall et al., 2021) have demonstrated high-fidelity novel view synthesis through an implicit representation, but constrained by slow optimization and limited geometric precision. In contrast, 3D Gaussian Splatting (3DGS) (Kerbl et al., 2023) leverages an explicit point-based representation to improve computational efficiency. Each Gaussian in 3DGS is characterized by parameters such as center, opacity, covariance, and color. Despite these improvements, the geometric accuracy and visual fidelity in 3DGS reconstructions can degrade under challenging conditions, such as motion-blurred or low-light environments (Zahid et al., 2025; Matta et al., 2025). To address these challenges, recent advancements in event-based 3DGS (Yura et al., 2025; Zhang et al., 2025) have shown promising results in enhancing reconstruction quality by utilizing event cameras. However, a notable gap in the existing works is the lack of relevant event dataset for large-scale 3D scene reconstruction. *To fill this gap, we introduce the first dataset specifically collected for event-enhanced UAV 3D scene reconstruction.*

2.2 Event-based 3D Reconstruction

Event cameras (Zheng et al., 2023; Xu et al., 2025) are bio-inspired sensors that capture asynchronous brightness changes, in contrast to traditional cameras, which capture images at a fixed frame rate. This unique sensing mechanism provides event cameras with distinct advantages, including exceptional temporal resolution, low latency, and resilience to motion blur and challenging lighting conditions. These attributes have spurred significant research into the application of event cameras across various computer vision tasks, such as object detection (Mitrokhin et al., 2018), depth estimation (Pan et al., 2024; Shi et al., 2023), semantic segmentation (Chen et al., 2024; Kong et al., 2024), video enhancement (Kim et al., 2024; Jing et al., 2021; Tulyakov et al., 2021), and, notably, 3D reconstruction (Chen et al., 2025; Wu et al., 2024; Cannici & Scaramuzza, 2024; Han et al., 2024; Cladera et al., 2025; Ye et al.; Han et al., 2024; Yu et al., 2025). In the domain of 3D reconstruction, early methods (Rudnev et al., 2023; Zhu et al., 2024; Low & Lee, 2023) combined NeRF with event-based data, utilizing volumetric rendering techniques guided by event supervision. More recent works (Zahid et al., 2025; Matta et al., 2025; Yura et al., 2025; Zhang et al., 2025)

have explored the integration of 3DGS with event data to enhance the reconstruction process. However, these prior approaches often face robustness issues, particularly in challenging conditions such as low-light and motion-blurred environments. To address these shortcomings, Dark-EvGS (Wu et al., 2025) introduces an event-based guided 3DGS pipeline, facilitating bright frame synthesis from arbitrary viewpoints in low-light scenarios. Although this approach represents a significant advancement, it remains primarily focused on small objects and does not fully capture the complexities of real-world 3D reconstruction tasks, which typically involve large-scale scenes. *In this work, we introduce a new dataset specifically designed for large-scale UAV 3D scene reconstruction, overcoming the limitations of previous methods in city-scale scenes.*

2.3 Comparison to Existing Event-guided Datasets

Early UAV-related event datasets, such as MVSEC (Zhu et al., 2018) and UZH-FPV (Delmerico et al., 2019), established important baselines by providing stereo events with aggressive flight trajectories and precise ground truth. However, these datasets are not curated for texture-rich, city-scale 3D modeling (e.g., limited image resolution/coverage and a focus on odometry rather than volumetric ground truth). Subsequent multi-platform corpora like M3ED (Chaney et al., 2023) include aerial sequences and synchronized modalities, but primarily target high-speed robotics rather than low-altitude urban reconstruction with dense geometry. The NU-AIR dataset (Iaboni et al., 2025) advances urban perception with aerial event streams and extensive detection labels, while lacking synchronized high-resolution RGB and per-frame dense depth required for neural rendering benchmarks. EvMAPPER (Cladera et al., 2025) represents a pioneering effort in event-based orthomapping at high altitudes, yet it generates only planar mosaics and does not capture the pose jitter and parallax needed for volumetric modeling at low altitudes. Beyond datasets focused on UAVs, event camera datasets and benchmarks from other domains, including automotive driving (Gehrig et al., 2021; Binas et al., 2017) and indoor robotics (Fischer & Milford, 2020; Mitrokhin et al.; Burner et al., 2022), have advanced event vision, but they are not tailored to aerial 3D reconstruction at city scale because they lack synchronized RGB, dense per-frame depth, and low altitude capture protocols. *To bridge this gap, in this work, we introduce event-enhanced UAV datasets tailored for large-scale 3D scene reconstruction.*

3 Dataset

We present SkyEvents, the first and large-scale UAV dataset that integrates tri-modal sensing across event camera streams, RGB videos, and LiDAR point clouds. This dataset spans five distinct environments, each characterized by unique architectural structures and diverse activity patterns. To address the critical challenge of accurate temporal synchronization across RGB and event data, we propose the Geometry-Constrained Timestamp Alignment (GTA) module. The GTA module ensures precise alignment of timestamps between event and RGB cameras, leveraging geometric constraints to optimize synchronization (see Figure 2).

3.1 Platform

To ensure the reproducibility and accessibility of our dataset collection methodology, we design a UAV sensor platform utilizing commercially available components and self-designed modules, shown in Figure 2, which lowers the barrier for community adoption and facilitates future extensions. The core platform leverages the DJI Matrice 350 RTK airframe for its positioning system with centimeter accuracy. The platform combines two complementary vision sensors: a Prophesee Gen4EVK event camera for high-speed event-based vision and a DJI Osmo Action 4 camera for standard RGB video. Besides, a Mini PC serves as the central on-board computing and data logging unit, handling raw data acquisition and temporary storage. More details are listed in Appendix Table 4.

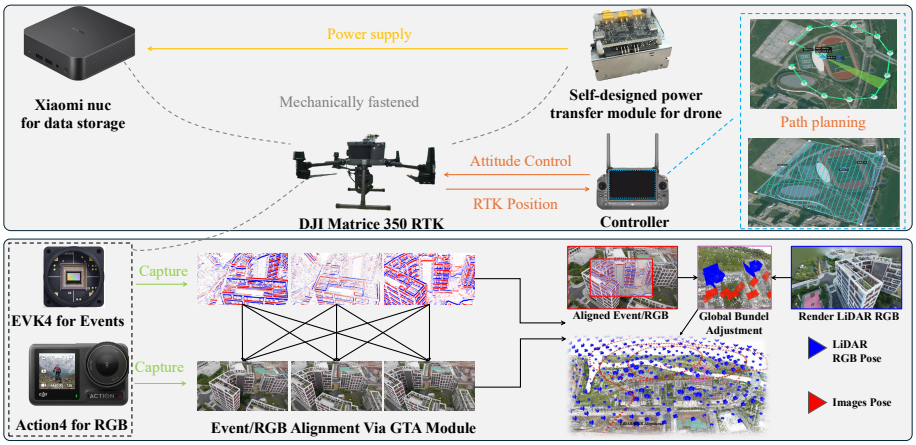

Figure 2: Data collection and rendering pipelines. The data acquisition platform consists of an UAV payload, an event camera, a 120HZ RGB camera, and a Mini PC. After collecting paired RGB and event data, we utilized the proposed Geometry-Constrained Timestamp Alignment (GTA) module to synchronize timestamps and warp between the event and RGB cameras.

3.2 Dataset Collection and Statistics

The platform receives control commands via a remote controller, supporting both real-time manual operation by a pilot and pre-loaded Keyhole Markup Language (KML) route plans. This flexibility enables two distinct flight strategies: (1) Circular orbits (21.4%) provide rapid data acquisition despite potential viewpoint gaps; while (2) automated four directional oblique scanning routes (78.6%) ensure systematic coverage at the cost of longer mission durations. Data acquisition is orchestrated by an onboard mini-PC, which runs a custom script that automatically arms recording once the UAV takes off. This script issues software triggers to start both the RGB camera and the event camera and logs their respective activation timestamps.

The comprehensive data statistics are shown in Figure 3, where our data collection encompasses a diverse set of environmental conditions and flight parameters. In detail, the drone platform executes missions across five distinct areas totaling 1.41 km^2, with flight altitudes strategically distributed at 70 m (51.7%), 100 m (41.3%), and 80 m (6.9%) to balance safety concerns with optimal sensor coverage. The dataset features extensive architectural variety, spanning complex buildings, medium-rise structures (8.2% area coverage), low-rise buildings (6.1%), open planar scenes (11.5%), and high-rise clusters (12.7%). Most data is collected under well-light daytime conditions (73.2%). Additionally, data at dusk (26.8%) is also collected in selected areas to enable validation under natural low-light environments.

Complementing the optical data, a DJI L2 LiDAR is deployed at approximately 100 meters for oblique photogrammetry across all areas. LiDAR point cloud is chosen to serve as the ground truth depth reference in this dataset owing to its superior accuracy. In total, 45 flight segments are conducted, accumulating approximately 8 hours of event and RGB video data, along with 0.72 km^2 of LiDAR point cloud data capturing at 2.64 cm/pixel GSD (see more details in Table 5 in Appendix).

3.3 Geometry-Constrained Timestamp Alignment

In our system, we observe that the event camera stream is typically delayed by approximately 5 ms relative to the RGB stream. Consequently, we need to ensure frame-accurate synchronization between event camera and RGB camera. Let $I_t \in \mathbb{R}^{H\times W\times 3}$ denote the RGB image at time t, and let $E_\tau \in \mathbb{R}^{H\times W\times 3}$ be the event-

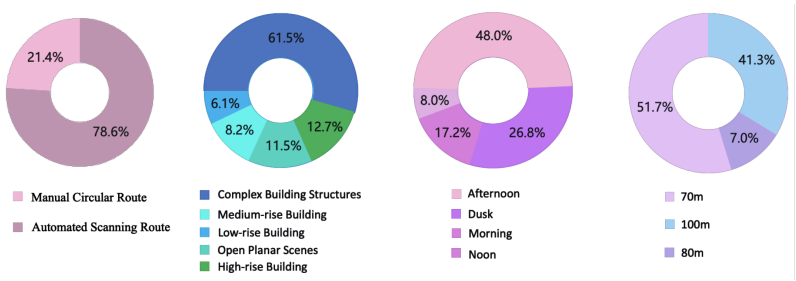

Figure 3: Data statistics from left to right: flight path, scenarios types, illumination, and height.

rendered image at time τ. Given RGB sampling times $\{t_k\}_{k=1}^{K}$ (e.g., 1s interval), we search a symmetric window $[t_k - \Delta,\ t_k + \Delta]$ with step δ and select the event time that maximizes a geometry score $\tau_k^\star$:

$$\tau_k^\star \in \arg\max_{\tau \in \mathcal{T}_k} S\big(I_{t_k}, E_\tau\big), \qquad \mathcal{T}_k = \{t_k - \Delta,\ t_k - \Delta + \delta, \ldots,\ t_k + \Delta\}. \tag{1}$$

where $\Delta = 100ms$ is the half-window size, $\delta = 8.333ms$ is the temporal step, $\mathcal{T}_k$ is the candidate set around t_k, and $S(\cdot, \cdot)$ is the geometry consistency score.

For a pair (E_τ, I_{t_k}), we obtain putative correspondences $\{(\mathbf{x}_i, \mathbf{x}_i')\}_{i=1}^{N}$ with $\mathbf{x}_i = (u_i, v_i) \in E_\tau$ and $\mathbf{x}_i' = (u_i', v_i') \in I_{t_k}$ via the dense matcher MatchAnything/ROMA (He et al., 2025; Edstedt et al., 2024), and estimate a robust homography $\mathbf{H} \in \mathbb{R}^{3\times3}$ from RGB to event via MAGSAC (Barath et al., 2019):

$$\lambda \begin{bmatrix} u \\ v \\ 1 \end{bmatrix} = \mathbf{H} \begin{bmatrix} u' \\ v' \\ 1 \end{bmatrix}, \qquad \lambda \neq 0. \tag{2}$$

where $\mathbf{H}$ maps RGB pixels to Event pixels, $[u, v, 1]^\top$ and $[u', v', 1]^\top$ are homogeneous coordinates in Event and RGB, and λ is the projective scale.

Let $\mathbf{m} \in \{0, 1\}^N$ be the inlier mask and $\Pi([x, y, w]^\top) = (x/w, y/w)$. The per-inlier reprojection error is $\varepsilon_i = \|\Pi(\mathbf{H}[\mathbf{x}_i'; 1]) - \mathbf{x}_i\|_2$. We then score the pair as

$$S\big(I_{t_k}, E_\tau\big) = \sum_{i=1}^{N} m_i \ - \ \alpha \frac{\sum_{i=1}^{N} m_i\, \varepsilon_i}{\max\big(1, \sum_{i=1}^{N} m_i\big)}, \qquad \alpha > 0, \tag{3}$$

where m_i indicates whether correspondence i is an inlier, ε_i is the Euclidean reprojection error for inlier i, and α balances inlier support and normalized error (invalid $\mathbf{H}$ yields a non-informative score).

To avoid per-pair perspective warping while preserving alignment, we approximate the RGB→Event homography $\mathbf{H}$ on a regular grid by a diagonal affine map $[x, y]^\top \approx \mathbf{D}[x', y']^\top + \mathbf{t}$ with $\mathbf{D} = \mathrm{diag}(s_x, s_y)$ and $\mathbf{t} = (t_x, t_y)^\top$, and estimate (s_x, s_y, t_x, t_y) via a *single linear least-squares fit*. Concretely, we sample M grid points (x_j', y_j') in RGB, project them to Event by $(x_j, y_j) = \Pi\big(\mathbf{H}[x_j', y_j', 1]^\top\big)$, and solve $\min_{\boldsymbol{\theta}} \|\mathbf{A}\boldsymbol{\theta} - \mathbf{b}\|_2^2$, where the unknown $\boldsymbol{\theta} = (s_x, t_x, s_y, t_y)^\top$, matrix $\mathbf{A}$ stacks RGB coordinates with axis-wise structure, and $\mathbf{b}$ stacks the corresponding Event coordinates (first all x_j, then all y_j). Given event and RGB resolutions (W_0, H_0) and (W_1, H_1), we derive an RGB crop window $(x_0, y_0) \to (x_1, y_1)$ by stabilizing scales with $\tilde{s}_x = \max(s_x, \epsilon)$, $\tilde{s}_y = \max(s_y, \epsilon)$, back-computing the crop origin from $(-t_x/\tilde{s}_x,\ -t_y/\tilde{s}_y)$ with clamping to valid bounds, and setting the crop size so that a bilinear resize matches the event resolution, i.e., widths/heights proportional to $W_0/\tilde{s}_x$ and $H_0/\tilde{s}_y$. We log $\mathbf{H}$, $\boldsymbol{\theta}$, and the crop coordinates for exact reproducibility, where $\epsilon > 0$ is a small stabilizer.

To enforce a global $1\,\mathrm{second}$ cadence and suppress local noise, we jointly refine the sequence by maximizing geometric consistency penalized by interval deviations:

$$\{\widetilde{\tau}_k\}_{k=1}^{K} = \arg\max_{\{\tau_k\}} \left[\sum_{k=1}^{K} S\big(I_{t_k}, E_{\tau_k}\big) - \beta \sum_{k=2}^{K} \big|(\tau_k - \tau_{k-1}) - 1\,\mathrm{s}\big| \right], \qquad \beta > 0. \tag{4}$$

where $\widetilde{\tau}_k$ are the refined event timestamps; β trades off the global $1\,\mathrm{second}$ cadence against geometric fit, and the absolute deviation term penalizes interval drift.

3.4 LiDAR Alignment

As demonstrated in Figure 2, we align LiDAR and RGB in a unified 3D coordinate and then transfer LiDAR geometry to each RGB image as metrically accurate depth. In our setup, a DJI Zenmuse L2 LiDAR payload and an RGB camera are flown in separate missions over the same area, so the raw trajectories are not temporally synchronized. To recover a consistent geometry, we adopt a unified structure-from-motion (SfM) pipeline using commercial photogrammetry software ***RealityScan***. We first rasterize the LiDAR point cloud into perspective "LiDAR RGB" images by projecting the laser returns onto virtual pinhole cameras whose intrinsics and extrinsics are derived from the LiDAR trajectory. RealityScan generates the poses of these LiDAR images, and we treat them as fixed anchor views. We then import the calibrated UAV RGB images and run joint SfM and global bundle adjustment over all images, keeping the LiDAR-derived camera poses frozen. This procedure rigidly registers all RGB cameras into the LiDAR coordinate system, yielding a single globally consistent Euclidean frame shared by LiDAR and RGB.

Given the optimized camera intrinsics and extrinsics, we perform a global multi-view stereo (MVS) reconstruction in which LiDAR depth acts as a strong geometric prior. Specifically, we fuse the LiDAR point cloud with MVS-derived depth estimates to obtain a dense, continuous mesh, where LiDAR stabilizes depth in texture-poor or repetitive regions and suppresses multi-view ambiguities. We treat this fused surface as the ground-truth (GT) geometry. Finally, for each RGB frame, we back-project the GT mesh into the corresponding camera using the calibrated intrinsics and extrinsics, producing dense, metrically accurate depth maps that are pixel-wise aligned with the original RGB images.

4 Benchmarks

4.1 Benchmark Method

To evaluate the effectiveness of incorporating event modality for 3D reconstruction, we leverage two state-of-the-art 3DGS pipelines, Luminance-GS (Cui et al., 2025) and Improved-GS (Deng et al., 2025), for benchmark experiments.

Input. Each event $e_i = (\mathbf{x}, t_i, p_i)$ is triggered at a microsecond timestamp t_i when the brightness at pixel $\mathbf{x}$ changes by more than a contrast threshold C (i.e., $|L(\mathbf{x}, t_{i+1}) - L(\mathbf{x}, t_i)| \geq C$), where $L(\mathbf{x}, t_i)$ is the logarithmic brightness, and $p_i \in \{-1, +1\}$ represents either an increase or decrease in the logarithmic brightness $L(\mathbf{x}, t_i)$. In parallel, RGB image I_{t_i} is captured at discrete time t_i.

4.2 Region-wise Event Rendering Loss

To encourage 3DGS to recover accurate geometry and appearance, we introduce an event-based brightness-change consistency loss Zhang et al. (2025). Given two timestamps t_1 and t_2, we accumulate events in this interval into an image $E(t_1, t_2) = \{e_i(\mathbf{x}, t_i, p_i)\}_{t_1 < t_i < t_2}$ and compare it with the synthesized brightness change, computed as the logarithmic difference between two rendered images $\hat{I}_{t_1}$ and $\hat{I}_{t_2}$. Since the

Scenes	Conditions	Methods	With Event			Without Event		
			SSIM↑	PSNR↑	LPIPS↓	SSIM↑	PSNR↑	LPIPS↓
Scene1	Low-light	Luminance-GS	0.1257	5.2060	0.5850	0.1214	4.7870	0.5990
	Blur	Improved-GS	0.8044	27.4368	0.2701	0.8095	27.3554	0.2757
		Improved-GS+kernel	0.8625	28.2600	0.2107	0.8655	28.1146	0.2045
Scene2	Low-light	Luminance-GS	0.1417	5.7650	0.5402	0.1408	5.7000	0.5411
	Blur	Improved-GS	0.7951	26.4789	0.2482	0.7807	25.8635	0.2653
		Improved-GS+kernel	0.2608	11.5674	0.6783	0.2488	11.5092	0.6816

Table 2: Rendering performance comparison across different conditions and scenarios, with and without event data.

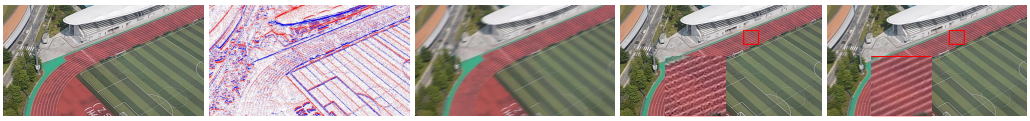

RGB Event Blurry RGB Improved-GS Improved-GS+RER

Figure 4: Comparison of 3D scene reconstruction with Improved-GS and Improved-GS+RER in blurred environments.

RGB and event sensors have different footprints and intrinsics, naively warping and undistorting RGB images leads to misalignment with the event frame. Instead, we estimate the warp between the two sensors and define a region-aligned event supervision loss that constrains the brightness change only within their overlapping regions. To ensure spatial support is consistent with the event frame, we apply the region-wise alignment and cropping derived in equation 1: we approximate the RGB→event homography by a diagonal affine map $\mathcal{C}_{\boldsymbol{\theta}}$ with parameters $\boldsymbol{\theta} = (s_x, s_y, t_x, t_y)$, derive a crop window, and resample to the event resolution. We then convert the aligned renderings to log space and define the loss as:

$$\mathcal{L}_{\text{event}} = \left\| \left(\log \mathcal{C}_{\boldsymbol{\theta}}(\hat{I}_{t_1}) - \log \mathcal{C}_{\boldsymbol{\theta}}(\hat{I}_{t_2})\right), E(t_1, t_2) \right\|_2 . \tag{5}$$

4.3 Implementation Details and Evaluation Metrics

Implementation Details. For the training setup, we employ Luminance-GS (Cui et al., 2025), a state-of-the-art (SOTA) 3DGS pipeline designed for complex illumination scenes, and Improved-GS (Deng et al., 2025), the SOTA neural rendering pipeline, to assess the effectiveness of incorporating event modality. Both models were trained on a single NVIDIA RTX 4090 using the Adam optimizer. Training is conducted for a total of 30,000 iterations, with Event refinement starting at 8,000 iterations. For other settings, such as Gaussian reset steps (Kerbl et al., 2023), we follow the default configuration.

Low-light Image Generation. Although UAVs can be programmed to repeat nearly identical RTK-guided flight paths across different light conditions, to build a unified model, we rely on structure-from-motion (SfM), which requires reliable feature detection and matching across views. Under low-light conditions, however, many images exhibit weak textures and low contrast, causing feature matching to fail. As a result, a substantial portion of low-light images cannot be registered in the SfM pipeline, preventing consistent multi-temporal 3D reconstruction. To evaluate performance of methods in low light-conditions, we utilize daytime sequences in our experiments and generate synthetic low-light versions. This ensures pixel-level correspondence, enabling controlled training and ablation studies. Following (Zhang et al., 2021; Liang et al., 2023), we generate low-light frames from corresponding normal-light frames using gamma correction and linear scaling, employing identical parameter settings. The process is formalized as follows: $L_t(p) = \beta \times (\alpha \times I_t(p))^{\gamma}$,where γ represents the gamma correction factor, which is sampled from a uniform distribution U(2, 3.5). The parameters α and β are linear scaling factors, drawn from U(0.9, 1) and U(0.5, 1), respectively.

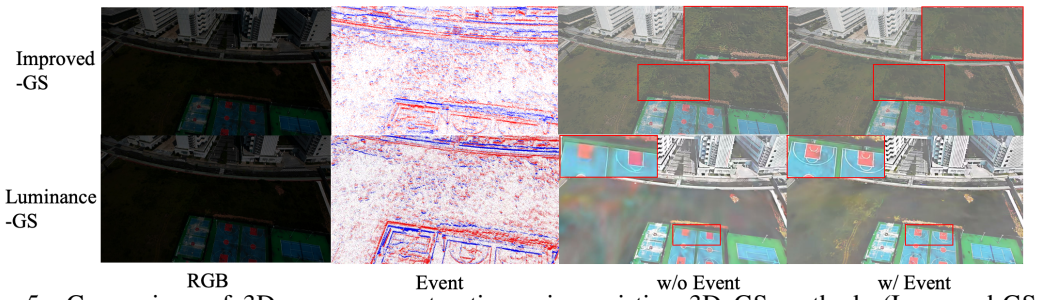

Figure 5: Comparison of 3D scene reconstruction using existing 3D GS methods (Improved-GS and Luminance-GS), with and without event enhancement. The integration of event modality through RER markedly enhances rendering quality.

Method	BRISQUE ↓	MANIQA ↑	NIQE ↓
E2VID	**7.1075**	0.2141	6.1096
E2VID+	7.3820	0.2842	5.4571
ET-Net	22.9103	0.2885	5.4518
FireNet	14.3349	0.2276	4.5584
FireNet+	12.7435	**0.3445**	**4.2509**
HyperE2VID	7.6182	0.2205	5.7398
SPADE-E2VID	14.7488	0.2444	7.0037
SSL-E2VID	59.9326	0.1701	9.0612

Table 3: Quantitative comparison of event-to-video methods.

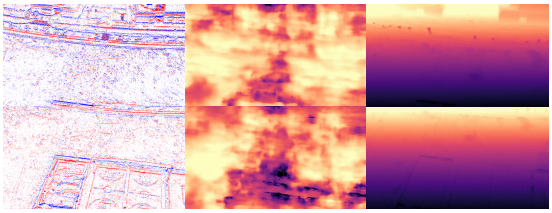

Figure 6: Depth Estimation.

Blurry Image Generation. Following prior work (Li et al., 2024), a motion-blurred image is physically generated by accumulating photons over the exposure time, ensuring that the resulting blurred image remains differentiable with respect to both the parameters of NeRF and the motion trajectory.

Evaluation Metrics. To thoroughly evaluate the performance of 3DGS methods, we employ standard quantitative metrics, including Peak Signal-to-Noise Ratio (PSNR), Structural Similarity Index Measure (SSIM), and Learned Perceptual Image Patch Similarity (LPIPS) (Zhang et al., 2018).

4.4 Results

In this section we focus on novel view synthesis from joint RGB and event input using three dimensional Gaussian splatting backbones. The goal is to answer a concrete question: *given a fixed rendering pipeline, does adding events improve reconstruction quality in low light and motion blurred UAV scenes?*

Table 2 summarizes the quantitative results on two representative scenes. For the low light setting with Luminance GS (Cui et al., 2025), events provide small but consistent gains. On both scenes, adding event supervision increases PSNR and slightly reduces LPIPS, while keeping SSIM essentially unchanged, which indicates that events act as a stabilizing cue under extreme illumination where RGB alone is severely underexposed. For the blurred setting with Improved GS (Cui et al., 2025), the benefit of events is more pronounced. On the larger Scene 2 with more than 800 training images, the gains are clearer: PSNR increases by about half a decibel and LPIPS decreases by a noticeable margin for the event driven model compared to the RGB only baseline. These trends hold both for the plain Improved GS variant and for the simple gamma recovery kernel, which shows that event cues remain helpful even when exposure is partially corrected on the RGB branch. Figure 4 visualizes the baseline comparison that underlies the blurred rows for Improved GS in Table 2. When events are used, double contours and ghosting around moving or blurred regions are notably reduced and details appear sharper, which matches the quantitative improvements in PSNR and

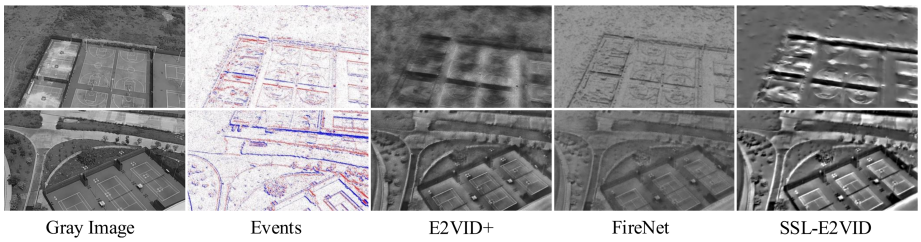

Figure 7: Video reconstruction performance comparison: E2VID+ (Stoffregen et al., 2020), FireNet (Scheerlinck et al., 2020), and SSL-E2VID (Paredes-Vallés & De Croon, 2021).

LPIPS. Under normal lighting, minor camera jitters that cause ambiguities in the RGB only reconstructions are also mitigated once event constraints are introduced.

Overall, these results suggest that events supply high-frequency constraints that particularly aid deblurring, and also benefit low-light reconstruction, especially in challenging or large-scale settings.

4.5 Other Tasks to Explore

Monocular Depth Estimation. We further evaluate event-based monocular depth estimation on SkyEvents by running inference with the SOTA E2Depth model. As illustrated in Figure 6, depth predictions exhibit noticeable artifacts and loss of fine structures in aerial event streams, highlighting that current models do not adequately address UAV-based event depth estimation and underlining the potential value of our dataset for this frontier task.

Event-to-Video Reconstruction. Table 3 and Figure 7 summarize the performance of representative event-to-video reconstruction methods on our SkyEvents dataset. Overall, methods originally trained on ground-level data struggle to generalize to UAV-based event streams. Methods such as ET-Net, SPADE-E2VID, and SSL-E2VID exhibit significantly degraded image quality, underscoring the challenge posed by our aerial, low-light event data and the need for dedicated training in this regime.

5 Conclusion

In this work, we introduced SkyEvents, the first large-scale, event-enhanced UAV dataset specifically designed for 3D scene reconstruction using RGB, event, and LiDAR data. The dataset spans a wide range of conditions, including variations in illumination, scenario, and flight height, comprising 45 sequences (over 8 hours) of paired RGB and event data, along with 0.72 km^2 of LiDAR point cloud data capturing at 2.64 cm/pixel GSD. To fully harness the potential of this large-scale dataset, we propose the Geometry-Constrained Timestamp Alignment (GTA) module, which effectively synchronizes timestamps between event and RGB camera data, and the Region-Wise Event Rendering (RER) loss, which guides the optimization of rendering. Experimental results underscore the significant contribution of event data to 3D scene reconstruction. In conclusion, we hope that SkyEvents will catalyze further research and innovation in the domain of event-enhanced 3D reconstruction, particularly in extreme scenarios.

Limitations and Future Work. Due to limitations in the current hardware setup, the RGB and event data are not perfectly aligned in both space and time. In the future, we aim to upgrade the data collection devices to obtain a larger, more precise, and higher-quality paired dataset, enabling more accurate synchronization under increasingly challenging and complex scenarios. This enhanced dataset will serve as a foundation for exploring a broader range of computer vision tasks, such as depth estimation and video frame interpolation.

REFERENCES

Daniel Barath, Jiri Matas, and Jana Noskova. MAGSAC: marginalizing sample consensus. In *Conference on Computer Vision and Pattern Recognition*, 2019.

Jonathan T Barron, Ben Mildenhall, Dor Verbin, Pratul P Srinivasan, and Peter Hedman. Mip-nerf 360: Unbounded anti-aliased neural radiance fields. In *Proceedings of the IEEE/CVF conference on computer vision and pattern recognition*, pp. 5470–5479, 2022.

Jonathan Binas, Daniel Neil, Shih-Chii Liu, and Tobi Delbruck. Ddd17: End-to-end davis driving dataset. *arXiv preprint arXiv:1711.01458*, 2017.

Levi Burner, Anton Mitrokhin, Cornelia Fermüller, and Yiannis Aloimonos. Evimo2: an event camera dataset for motion segmentation, optical flow, structure from motion, and visual inertial odometry in indoor scenes with monocular or stereo algorithms. *arXiv preprint arXiv:2205.03467*, 2022.

Pablo Rodrigo Gantier Cadena, Yeqiang Qian, Chunxiang Wang, and Ming Yang. Spade-e2vid: Spatially-adaptive denormalization for event-based video reconstruction. *IEEE Transactions on Image Processing*, 30:2488–2500, 2021.

Marco Cannici and Davide Scaramuzza. Mitigating motion blur in neural radiance fields with events and frames. In *Proceedings of the IEEE/CVF Conference on Computer Vision and Pattern Recognition*, pp. 9286–9296, 2024.

Kenneth Chaney, Fernando Cladera, Ziyun Wang, Anthony Bisulco, M Ani Hsieh, Christopher Korpela, Vijay Kumar, Camillo J Taylor, and Kostas Daniilidis. M3ed: Multi-robot, multi-sensor, multi-environment event dataset. In *Proceedings of the IEEE/CVF Conference on Computer Vision and Pattern Recognition*, pp. 4016–4023, 2023.

Zehao Chen, Zhanfeng Liao, De Ma, Huajin Tang, Qian Zheng, and Gang Pan. Evhdr-nerf: Building high dynamic range radiance fields with single exposure images and events. In *Proceedings of the AAAI Conference on Artificial Intelligence*, volume 39, pp. 2376–2384, 2025.

Zhiwen Chen, Zhiyu Zhu, Yifan Zhang, Junhui Hou, Guangming Shi, and Jinjian Wu. Segment any event streams via weighted adaptation of pivotal tokens. In *Proceedings of the IEEE/CVF Conference on Computer Vision and Pattern Recognition*, pp. 3890–3900, 2024.

Fernando Cladera, Kenneth Chaney, M Ani Hsieh, Camillo J Taylor, and Vijay Kumar. Evmapper: High-altitude orthomapping with event cameras. In *2025 IEEE International Conference on Robotics and Automation (ICRA)*, pp. 310–316. IEEE, 2025.

Ziteng Cui, Xuangeng Chu, and Tatsuya Harada. Luminance-gs: Adapting 3d gaussian splatting to challenging lighting conditions with view-adaptive curve adjustment. In *Proceedings of the IEEE/CVF Conference on Computer Vision and Pattern Recognition (CVPR)*, pp. 26472–26482, June 2025.

Jeffrey Delmerico, Titus Cieslewski, Henri Rebecq, Matthias Faessler, and Davide Scaramuzza. Are we ready for autonomous drone racing? the uzh-fpv drone racing dataset. In *2019 International Conference on Robotics and Automation (ICRA)*, pp. 6713–6719. IEEE, 2019.

Kangle Deng, Andrew Liu, Jun-Yan Zhu, and Deva Ramanan. Depth-supervised nerf: Fewer views and faster training for free. In *Proceedings of the IEEE/CVF conference on computer vision and pattern recognition*, pp. 12882–12891, 2022.

Xiaobin Deng, Changyu Diao, Min Li, Ruohan Yu, and Duanqing Xu. Improving densification in 3d gaussian splatting for high-fidelity rendering. *arXiv preprint arXiv:2508.12313*, 2025.

Johan Edstedt, Qiyu Sun, Georg Bökman, Mårten Wadenbäck, and Michael Felsberg. RoMa: Robust Dense Feature Matching. *IEEE Conference on Computer Vision and Pattern Recognition*, 2024.

Burak Ercan, Onur Eker, Canberk Saglam, Aykut Erdem, and Erkut Erdem. Hypere2vid: Improving event-based video reconstruction via hypernetworks. *IEEE Transactions on Image Processing*, 33:1826–1837, 2024.

Tobias Fischer and Michael Milford. Event-based visual place recognition with ensembles of temporal windows. *IEEE Robotics and Automation Letters*, 5(4):6924–6931, 2020.

Stephan J Garbin, Marek Kowalski, Matthew Johnson, Jamie Shotton, and Julien Valentin. Fastnerf: High-fidelity neural rendering at 200fps. In *Proceedings of the IEEE/CVF international conference on computer vision*, pp. 14346–14355, 2021.

Mathias Gehrig, Willem Aarents, Daniel Gehrig, and Davide Scaramuzza. Dsec: A stereo event camera dataset for driving scenarios. *IEEE Robotics and Automation Letters*, 6(3):4947–4954, 2021.

Antoine Guédon and Vincent Lepetit. Sugar: Surface-aligned gaussian splatting for efficient 3d mesh reconstruction and high-quality mesh rendering. *arXiv preprint arXiv:2311.12775*, 2023.

Hanqian Han, Jianing Li, Henglu Wei, and Xiangyang Ji. Event-3dgs: Event-based 3d reconstruction using 3d gaussian splatting. *Advances in Neural Information Processing Systems*, 37:128139–128159, 2024.

Xingyi He, Hao Yu, Sida Peng, Dongli Tan, Zehong Shen, Hujun Bao, and Xiaowei Zhou. Matchanything: Universal cross-modality image matching with large-scale pre-training. In *Arxiv*, 2025.

Binbin Huang, Zehao Yu, Anpei Chen, Andreas Geiger, and Shenghua Gao. 2d gaussian splatting for geometrically accurate radiance fields. In *SIGGRAPH 2024 Conference Papers*. Association for Computing Machinery, 2024. doi: 10.1145/3641519.3657428.

Craig Iaboni, Thomas Kelly, and Pramod Abichandani. Nu-air: A neuromorphic urban aerial dataset for detection and localization of pedestrians and vehicles. *International Journal of Computer Vision*, pp. 1–19, 2025.

Yongcheng Jing, Yiding Yang, Xinchao Wang, Mingli Song, and Dacheng Tao. Turning frequency to resolution: Video super-resolution via event cameras. In *Proceedings of the IEEE/CVF Conference on Computer Vision and Pattern Recognition*, pp. 7772–7781, 2021.

Bernhard Kerbl, Georgios Kopanas, Thomas Leimkühler, and George Drettakis. 3d gaussian splatting for real-time radiance field rendering. *ACM Trans. Graph.*, 42(4):139–1, 2023.

Taewoo Kim, Jaeseok Jeong, Hoonhee Cho, Yuhwan Jeong, and Kuk-Jin Yoon. Towards real-world event-guided low-light video enhancement and deblurring. In *European Conference on Computer Vision*, pp. 433–451. Springer, 2024.

Lingdong Kong, Youquan Liu, Lai Xing Ng, Benoit R Cottereau, and Wei Tsang Ooi. Openess: Event-based semantic scene understanding with open vocabularies. In *Proceedings of the IEEE/CVF Conference on Computer Vision and Pattern Recognition*, pp. 15686–15698, 2024.

Wenpu Li, Pian Wan, Peng Wang, Jinghang Li, Yi Zhou, and Peidong Liu. Benerf: neural radiance fields from a single blurry image and event stream. In *European Conference on Computer Vision*, pp. 416–434. Springer, 2024.

Zhaoshuo Li, Thomas Müller, Alex Evans, Russell H Taylor, Mathias Unberath, Ming-Yu Liu, and Chen-Hsuan Lin. Neuralangelo: High-fidelity neural surface reconstruction. In *Proceedings of the IEEE/CVF Conference on Computer Vision and Pattern Recognition*, pp. 8456–8465, 2023.

Zhuoxiao Li, Shanliang Yao, Taoyu Wu, Yong Yue, Wufan Zhao, Rongjun Qin, Angel F. Garcia-Fernandez, Andrew Levers, and Xiaohui Zhu. Ulsr-gs: Ultra large-scale surface reconstruction gaussian splatting with multi-view geometric consistency, 2025. URL https://arxiv.org/abs/2412.01402.

Jinxiu Liang, Yixin Yang, Boyu Li, Peiqi Duan, Yong Xu, and Boxin Shi. Coherent event guided low-light video enhancement. In *Proceedings of the IEEE/CVF International Conference on Computer Vision*, pp. 10615–10625, 2023.

Jiaqi Lin, Zhihao Li, Xiao Tang, Jianzhuang Liu, Shiyong Liu, Jiayue Liu, Yangdi Lu, Xiaofei Wu, Songcen Xu, Youliang Yan, and Wenming Yang. Vastgaussian: Vast 3d gaussians for large scene reconstruction. In *CVPR*, 2024.

Yang Liu, Chuanchen Luo, Zhongkai Mao, Junran Peng, and Zhaoxiang Zhang. Citygaussianv2: Efficient and geometrically accurate reconstruction for large-scale scenes. In *ICLR*, 2025.

Weng Fei Low and Gim Hee Lee. Robust e-nerf: Nerf from sparse & noisy events under non-uniform motion. In *Proceedings of the IEEE/CVF International Conference on Computer Vision*, pp. 18335–18346, 2023.

Gopi Raju Matta, Trisha Reddypalli, and Kaushik Mitra. Besplat: Gaussian splatting from a single blurry image and event stream. In *Proceedings of the Winter Conference on Applications of Computer Vision*, pp. 917–927, 2025.

Zhenxing Mi and Dan Xu. Switch-nerf: Learning scene decomposition with mixture of experts for large-scale neural radiance fields. In *International Conference on Learning Representations (ICLR)*, 2023. URL https://openreview.net/forum?id=PQ2zoIZqvm.

Ben Mildenhall, Pratul P Srinivasan, Matthew Tancik, Jonathan T Barron, Ravi Ramamoorthi, and Ren Ng. Nerf: Representing scenes as neural radiance fields for view synthesis. *Communications of the ACM*, 65 (1):99–106, 2021.

Anton Mitrokhin, Chengxi Ye, Cornelia Fermüller, Yiannis Aloimonos, and Tobi Delbruck. Ev-imo: Motion segmentation dataset and learning pipeline for event cameras. in 2019 ieee. In *RSJ International Conference on Intelligent Robots and Systems (IROS)*, pp. 6105–6112.

Anton Mitrokhin, Cornelia Fermüller, Chethan Parameshwara, and Yiannis Aloimonos. Event-based moving object detection and tracking. In *2018 IEEE/RSJ International Conference on Intelligent Robots and Systems (IROS)*, pp. 1–9. IEEE, 2018.

Thomas Müller, Alex Evans, Christoph Schied, and Alexander Keller. Instant neural graphics primitives with a multiresolution hash encoding. *ACM Trans. Graph.*, 41(4):102:1–102:15, July 2022. doi: 10.1145/3528223.3530127. URL https://doi.org/10.1145/3528223.3530127.

Tianbo Pan, Zidong Cao, and Lin Wang. Srfnet: Monocular depth estimation with fine-grained structure via spatial reliability-oriented fusion of frames and events. In *2024 IEEE International Conference on Robotics and Automation (ICRA)*, pp. 10695–10702. IEEE, 2024.

Federico Paredes-Vallés and Guido CHE De Croon. Back to event basics: Self-supervised learning of image reconstruction for event cameras via photometric constancy. In *Proceedings of the IEEE/CVF Conference on Computer Vision and Pattern Recognition*, pp. 3446–3455, 2021.

Henri Rebecq, René Ranftl, Vladlen Koltun, and Davide Scaramuzza. Events-to-video: Bringing modern computer vision to event cameras. In *Proceedings of the IEEE/CVF Conference on Computer Vision and Pattern Recognition*, pp. 3857–3866, 2019.

Viktor Rudnev, Mohamed Elgharib, Christian Theobalt, and Vladislav Golyanik. Eventnerf: Neural radiance fields from a single colour event camera. In *Proceedings of the IEEE/CVF Conference on Computer Vision and Pattern Recognition*, pp. 4992–5002, 2023.

Cedric Scheerlinck, Henri Rebecq, Daniel Gehrig, Nick Barnes, Robert Mahony, and Davide Scaramuzza. Fast image reconstruction with an event camera. In *Proceedings of the IEEE/CVF Winter Conference on Applications of Computer Vision*, pp. 156–163, 2020.

Peilun Shi, Jiachuan Peng, Jianing Qiu, Xinwei Ju, Frank Po Wen Lo, and Benny Lo. Even: An event-based framework for monocular depth estimation at adverse night conditions. In *2023 IEEE International Conference on Robotics and Biomimetics (ROBIO)*, pp. 1–7. IEEE, 2023.

Timo Stoffregen, Cedric Scheerlinck, Davide Scaramuzza, Tom Drummond, Nick Barnes, Lindsay Kleeman, and Robert Mahony. Reducing the sim-to-real gap for event cameras. In *European Conference on Computer Vision*, pp. 534–549. Springer, 2020.

Matthew Tancik, Vincent Casser, Xinchen Yan, Sabeek Pradhan, Ben Mildenhall, Pratul Srinivasan, Jonathan T. Barron, and Henrik Kretzschmar. Block-NeRF: Scalable large scene neural view synthesis. *arXiv*, 2022.

Stepan Tulyakov, Daniel Gehrig, Stamatios Georgoulis, Julius Erbach, Mathias Gehrig, Yuanyou Li, and Davide Scaramuzza. Time lens: Event-based video frame interpolation. In *Proceedings of the IEEE/CVF conference on computer vision and pattern recognition*, pp. 16155–16164, 2021.

Haithem Turki, Deva Ramanan, and Mahadev Satyanarayanan. Mega-nerf: Scalable construction of large-scale nerfs for virtual fly-throughs. In *Proceedings of the IEEE/CVF Conference on Computer Vision and Pattern Recognition*, pp. 12922–12931, 2022.

Wenming Weng, Yueyi Zhang, and Zhiwei Xiong. Event-based video reconstruction using transformer. In *Proceedings of the IEEE/CVF International Conference on Computer Vision*, pp. 2563–2572, 2021.

Jingqian Wu, Shuo Zhu, Chutian Wang, Boxin Shi, and Edmund Y Lam. Sweepevgs: Event-based 3d gaussian splatting for macro and micro radiance field rendering from a single sweep. *arXiv preprint arXiv:2412.11579*, 2024.

Jingqian Wu, Peiqi Duan, Zongqiang Wang, Changwei Wang, Boxin Shi, and Edmund Y Lam. Dark-evgs: Event camera as an eye for radiance field in the dark. *arXiv preprint arXiv:2507.11931*, 2025.

Chuanzhi Xu, Haoxian Zhou, Langyi Chen, Haodong Chen, Ying Zhou, Vera Chung, Qiang Qu, and Weidong Cai. A survey of 3d reconstruction with event cameras. *arXiv preprint arXiv:2505.08438*, 2025.

Qinghong Ye, Yiqian Chang, Jianing Li, Haoran Xu, Xuan Wang, Wei Zhang, Yonghong Tian, and Peixi Peng. Spike4dgs: Towards high-speed dynamic scene rendering with 4d gaussian splatting via a spike camera array. In *The Thirty-ninth Annual Conference on Neural Information Processing Systems*.

Wangbo Yu, Chaoran Feng, Jianing Li, Jiye Tang, Jiashu Yang, Zhenyu Tang, Meng Cao, Xu Jia, Yuchao Yang, Li Yuan, et al. Evagaussians: Event stream assisted gaussian splatting from blurry images. In *Proceedings of the IEEE/CVF International Conference on Computer Vision*, pp. 24780–24790, 2025.

Zehao Yu, Anpei Chen, Binbin Huang, Torsten Sattler, and Andreas Geiger. Mip-splatting: Alias-free 3d gaussian splatting. In *Proceedings of the IEEE/CVF Conference on Computer Vision and Pattern Recognition*, pp. 19447–19456, 2024.

Gim Hee Lee Yu Chen. Dogaussian: Distributed-oriented gaussian splatting for large-scale 3d reconstruction via gaussian consensus. In *arXiv*, 2024.

Toshiya Yura, Ashkan Mirzaei, and Igor Gilitschenski. Eventsplat: 3d gaussian splatting from moving event cameras for real-time rendering. In *Proceedings of the Computer Vision and Pattern Recognition Conference*, pp. 26876–26886, 2025.

Sohaib Zahid, Viktor Rudnev, Eddy Ilg, and Vladislav Golyanik. E-3dgs: Event-based novel view rendering of large-scale scenes using 3d gaussian splatting. *arXiv preprint arXiv:2502.10827*, 2025.

Fan Zhang, Yu Li, Shaodi You, and Ying Fu. Learning temporal consistency for low light video enhancement from single images. In *Proceedings of the IEEE/CVF conference on computer vision and pattern recognition*, pp. 4967–4976, 2021.

Richard Zhang, Phillip Isola, Alexei A Efros, Eli Shechtman, and Oliver Wang. The unreasonable effectiveness of deep features as a perceptual metric. In *Proceedings of the IEEE conference on computer vision and pattern recognition*, pp. 586–595, 2018.

Zixin Zhang, Kanghao Chen, and Lin Wang. Elite-evgs: Learning event-based 3d gaussian splatting by distilling event-to-video priors. In *2025 IEEE International Conference on Robotics and Automation (ICRA)*, pp. 13972–13978. IEEE, 2025.

Xu Zheng, Yexin Liu, Yunfan Lu, Tongyan Hua, Tianbo Pan, Weiming Zhang, Dacheng Tao, and Lin Wang. Deep learning for event-based vision: A comprehensive survey and benchmarks. *arXiv preprint arXiv:2302.08890*, 2023.

Alex Zihao Zhu, Dinesh Thakur, Tolga Özaslan, Bernd Pfrommer, Vijay Kumar, and Kostas Daniilidis. The multivehicle stereo event camera dataset: An event camera dataset for 3d perception. *IEEE Robotics and Automation Letters*, 3(3):2032–2039, 2018.

Lin Zhu, Kangmin Jia, Yifan Zhao, Yunshan Qi, Lizhi Wang, and Hua Huang. Spikenerf: Learning neural radiance fields from continuous spike stream. In *Proceedings of the IEEE/CVF Conference on Computer Vision and Pattern Recognition*, pp. 6285–6295, 2024.

A APPENDIX

A.1 UAV PLATFORM & SENSOR SYSTEM DESIGN

The data acquisition system was built around a DJI Matrice 350 RTK unmanned aerial vehicle, selected for its robust payload capacity of 2.7 kg and extended flight endurance of approximately 45 minutes, shown in Figure 8. This platform integrates RTK GNSS positioning with centimeter-level accuracy, ensuring precise georeferencing throughout all missions. The airframe's IP55 weather resistance enables operations under varying environmental conditions.

(a) Front view (b) Side view (c) Rear view

Figure 8: Multi-modal UAV data collection platform overview. The DJI Matrice 350 RTK is equipped with a synchronized sensor suite and An onboard mini-PC.

A custom-designed sensor suite was mounted on a vibration-damped carbon fiber plate to minimize motion artifacts, shown in Figure 9. The core vision system consists of two synchronized cameras: a Prophesee EVK4 HD event camera capturing asynchronous events at 1280×720 resolution with sub-millisecond latency, and a DJI Osmo Action 4 RGB camera recording 4K video at 120 fps with global shutter. Temporal alignment between these sensors was maintained with microsecond-level precision.

A.2 DATA COLLECTION SYSTEM KEY COMPONENTS

An onboard Xiaomi Mini PC served as the central computing unit, handling real-time data acquisition from both cameras through USB 3.2 interfaces. With sustained write speeds exceeding 500 MB/s, this system reliably captured the high-bandwidth event streams (up to 10 Mevts/s) alongside uncompressed RGB video. The complete setup represents a balanced integration of commercial components and custom mounting solutions, providing a reproducible platform for multi-modal aerial data collection across diverse urban environments. Platform detail are listed in Table 4

A.3 LARGE-SCALE SCENARIO DIVERSITY

The dataset encompasses five distinct scenes at Hong Kong University of Science and Technology (Guangzhou), shown in Figure 10, captured in sequential order: **(1) Main Teaching Building (2) North Dormitory, (3) Data Center, (4) Sports Field, (5) South Dormitory**. Details are listed in Figure 10 and Table 1 and each scene presents unique architectural and environmental challenges for aerial perception:

- **Main Teaching Complex**: A vast interconnected structure comprising ∼10 buildings with glass facades, featuring a central aerial garden with dense foliage, ground-level water bodies, and tree clusters.

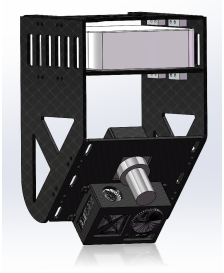

(a) Carbon fiber mounting plate

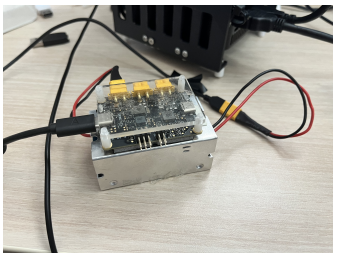

(b) Power conversion module

(c) Flight controller with route planning

Figure 9: Key components of the UAV data collection system. (a) Custom carbon fiber plate provides rigid mounting for sensors and computing unit while damping vibrations. (b) Power conversion module regulates DJI battery output to stable 12V/5V for onboard electronics. (c) Remote controller with pre-loaded KML routes enables fully autonomous flight operations.

- **North/South Dormitories**: High-rise residential buildings with rich texture patterns. The North Dormitory was sampled at around 70m, while the taller South Dormitory required 100m flight altitude for comprehensive coverage. Both feature intricate shadow dynamics from vertical structures.
- **Data Center**: Three isolated white-toned buildings with minimal color variation, creating texture-poor surfaces ideal for testing feature extraction algorithms. Uniform 70m sampling height.
- **Sports Field**: Complementary low-texture environments characterized by monochromatic surfaces. The outdoor Sports Field features uniform turf patterns, while the indoor Gymnasium contains fast-moving human activities under variable artificial lighting.

A.4 Matching Results

Figure 11 shows the matching results with the proposed GTA module on SkyEvents and MVSEC datasets. And as shown in the figure, the event streams aligned by our GTA module exhibit a pixel-perfect correspondence with the RGB frames' geometric edges. Moreover, the successful alignment on MVSEC confirms that our module generalizes well and achieves high temporal precision.

A.5 Other Tasks to Explore

Figure 13 shows the performance of existing event-to-video reconstruction methods E2VID (Rebecq et al., 2019), E2VID+ (Stoffregen et al., 2020), FireNet (Scheerlinck et al., 2020), ET-Net (Weng et al., 2021), FireNet+ (Stoffregen et al., 2020), HyperE2VID (Ercan et al., 2024), SPADE-E2VID (Cadena et al., 2021), and SSL-E2VID (Paredes-Vallés & De Croon, 2021) when applied to our SkyEvents dataset.

Figure 10: Campus region overview. The map shows five distinct areas: (1) Main Building complex, (2) North Dormitory, (3) Data Center, (4) Playground, and (5) South Dormitory, covering diverse urban scenarios for multi-modal data collection.

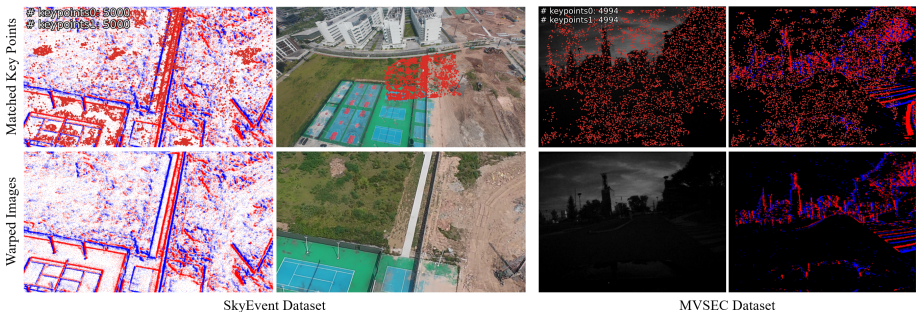

Figure 11: Matching results with the proposed GTA module on SkyEvents and MVSEC datasets.

Table 4: Precise Sensor Suite Specifications and Integration Details

DJI Matrice 350 RTK (UAV Platform)	
Category	**Specification / Details**
Role	Primary aerial vehicle
Dimensions	**Folded**: 430 × 420 × 430 mm (with props) **Unfolded**: 810 × 670 × 430 mm
Weight	**Without battery**: 3.77 kg; **With dual battery**: 6.47 kg
Payload	**Capacity**: 2.7 kg (max takeoff weight 9.2 kg); **Gimbal load**: 960 g max
Flight	**Endurance**: ∼55 min (unloaded, 8 m/s cruise) **Max speed**: 23 m/s (horizontal), 6 m/s (ascent), 5 m/s (descent) **Rotation rate**: Pitch: 300°/s, Yaw: 100°/s
Positioning	**System**: RTK GNSS (GPS+GLONASS+BeiDou+Galileo); **Accuracy**: 1 cm +1 ppm (horiz), 1.5 cm +1 ppm (vert)
Environmental	**Rating**: IP55 (weather resistant); **Max altitude**: 5000 m (with 2110s props)
Safety	ADS-B receiver, dual battery redundancy
Integration	Custom vibration-damped carbon fiber plate
Prophesee EVK4 HD (Event Camera)	
Category	**Specification / Details**
Role	Asynchronous event capture
Resolution	1280 × 720 (HD)
Pixel size	4.86 × 4.86 μm
Temporal	**Latency**: 220 μs; **Event Rate**: 10 Mevts/s (million events per second)
Dynamic Range	86 dB (up to 120 dB under low light)
Spectral	**Response**: 400-1000 nm (visible to NIR)
Power	**Consumption**: 0.5 W (USB powered)
Interface	**Data**: USB 3.0 Type-C; **Sync**: IX Connector Type B (sync in/out, trigger in)
Mechanical	**Dimensions**: 30 × 30 × 36 mm; **Weight**: 40 g (excluding lens)
Mounting	Rigid co-location with RGB camera
Optics	**Included**: C-mount 1/2.5" lens (FOV 47.7°)
Calibration	Temporal-spatial calibration with RGB
DJI Osmo Action 4 (RGB Camera)	
Category	**Specification / Details**
Role	Synchronized RGB video capture
Resolution	4K UHD (3840 × 2160) @ 120 fps
Shutter	Global shutter (eliminates rolling shutter artifacts)
Sensor	**Size**: 1/1.3" CMOS; **Pixel Size**: 2.4 μm
Dynamic Range	D-Log M (10-bit color depth)
Lens	**FOV**: 155°(wide mode)
Synchronization	**Accuracy**: $<$100 μs relative to event camera
Xiaomi Mini PC (Compute & Data Logger)	
Category	**Specification / Details**
Role	Central data acquisition hub
CPU	Intel N100 (4-core, 3.4GHz Turbo)
Memory	16GB DDR4 RAM
Storage	512GB NVMe SSD
I/O	**Ports**: 4 × USB 3.2 Gen 2 (10Gbps), 1 × HDMI 2.0, 1 × 2.5G Ethernet
OS	Windows 10 Professional
Power	**Consumption**: 12W TDP (powered via UAV battery)
Data Rate	**Capacity**: ∼500 MB/s sustained write

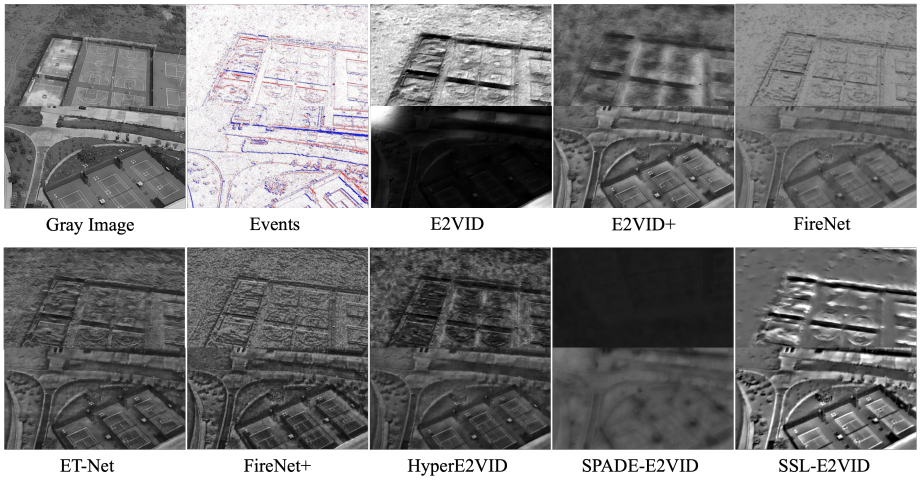

Figure 12: Video reconstruction with E2VID, E2VID+, FireNet, ET-Net, FireNet+, HyperE2VID, SPADE-E2VID, and SSL-E2VID.

A.6 DATASET STATISTICS AND EXAMPLES

A.6.1 DATASET STATISTICS

The SkyEvents dataset comprises multi-modal aerial data collected across five distinct urban scenarios, including complex building structures, low-rise and high-rise buildings, and open planar scenes. Data acquisition was performed using a UAV platform equipped with synchronized RGB (3840×2160), event (1280×720), and LiDAR sensors. Flights were conducted at altitudes of 70–100 m under varied illumination conditions (morning, noon, afternoon, dusk), with both automated routes and manual circular paths employed to ensure comprehensive spatial coverage. The dataset spans a total duration of 28,866 seconds, amounting to 2.02 TB of data. Detailed specifications for each sequence—including sensor types, illumination, resolution, flight parameters, and data size—are summarized in Table 5. This diverse collection supports development and evaluation of perception algorithms under real-world urban scenarios.

Table 5: SkyEvents Dataset Collection Statistics

Sequence	Sensor	Illumin.	Dur.(s)	Resolution	Scenario	Flight Path	Height(m)	Data Size(GB)
07061519	RGB	Afternoon	1056	3840×2160	Medium-rise building	Auto flight	70	16.00
07061519	Event	Afternoon	1435	1280×720	Medium-rise building	Auto flight	70	115.00
07061537	RGB	Afternoon	379	3840×2160	Medium-rise building	Auto flight	70	5.54
07061635	RGB	Afternoon	1056	3840×2160	Low-rise building	Auto flight	70	16.00
07061635	Event	Afternoon	1056	1280×720	Low-rise building	Auto flight	70	141.00
07071011	RGB	Morning	1056	3840×2160	Open planar scenes	Auto flight	70	16.00
07071011	Event	Morning	1523	1280×720	Open planar scenes	Auto flight	70	103.00
07071029	RGB	Morning	467	3840×2160	Open planar scenes	Auto flight	70	7.04
07071146	RGB	Noon	1056	3840×2160	High-rise building	Auto flight	100	16.00
07071146	Event	Morning	1820	1280×720	High-rise building	Auto flight	100	150.00
07071204	RGB	Noon	764	3840×2160	High-rise building	Auto flight	100	11.50
07071500	RGB	Afternoon	1056	3840×2160	Complex building	Auto flight	100	16.00
07071500	Event	Afternoon	1628	1280×720	Complex building	Auto flight	100	145.00
07071518	RGB	Afternoon	572	3840×2160	Complex building	Auto flight	100	8.68
07071631	Event	Afternoon	1618	1280×720	Complex building	Auto flight	100	139.00
07071632	RGB	Afternoon	1056	3840×2160	Complex building	Auto flight	100	16.00
07071649	RGB	Afternoon	562	3840×2160	Complex building	Auto flight	100	8.47
07071800	RGB	Dusk	1056	3840×2160	Low-rise building	Auto flight	70	16.00
07071800	Event	Dusk	1183	1280×720	Low-rise building	Auto flight	70	95.70
07071817	RGB	Dusk	127	3840×2160	Open planar scenes	Auto flight	70	1.92
07071936	RGB	Dusk	1454	3840×2160	Medium-rise building	Auto flight	70	13.40
07071936	Event	Dusk	1454	1280×720	Medium-rise building	Auto flight	70	40.20
09111836	RGB	Dusk	546	3840×2160	Complex building	Manual circle	70	8.21
09111836	Event	Dusk	546	1280×720	Complex building	Manual circle	70	7.89
09121548	RGB	Afternoon	969	3840×2160	Open planar scenes	Manual circle	80	14.50
09121549	Event	Afternoon	969	1280×720	Open planar scenes	Manual circle	80	12.80
09121611	RGB	Afternoon	911	3840×2160	Open planar scenes	Auto flight	80	13.60
09121612	Event	Afternoon	911	1280×720	Open planar scenes	Auto flight	80	30.40
09141514	RGB	Afternoon	1053	3840×2160	Complex building	Auto flight	100	16.00
09141514	Event	Afternoon	1913	1280×720	Complex building	Auto flight	100	72.50
09141532	RGB	Afternoon	860	3840×2160	Complex building	Auto flight	100	12.40
09141551	RGB	Afternoon	752	3840×2160	Complex building	Auto flight	100	10.80
09141551	Event	Afternoon	752	1280×720	Complex building	Auto flight	100	23.80
09141605	RGB	Afternoon	1066	3840×2160	Complex building	Manual circle	80	15.90
09141605	Event	Afternoon	1066	1280×720	Complex building	Manual circle	80	56.30
09141759	RGB	Dusk	1053	3840×2160	Complex building	Auto flight	100	16.00
09141759	Event	Dusk	1803	1280×720	Complex building	Auto flight	100	104.00
09141816	RGB	Dusk	750	3840×2160	Complex building	Auto flight	100	10.90
09191513	RGB	Afternoon	782	3840×2160	Low-rise building	Manual circle	100	11.30
09191513	Event	Afternoon	782	1280×720	Low-rise building	Manual circle	100	22.80
09191530	RGB	Afternoon	599	3840×2160	Medium-rise building	Manual circle	100	8.76
09191530	Event	Afternoon	599	1280×720	Medium-rise building	Manual circle	100	24.10
09191543	RGB	Afternoon	1053	3840×2160	High-rise building	Manual circle	100	16.00
09191543	Event	Afternoon	1208	1280×720	High-rise building	Manual circle	100	52.20
09191601	RGB	Afternoon	155	3840×2160	High-rise building	Manual circle	100	2.08
0922	LiDAR	-	6600	-	All regions	Auto flight	100	362.00
Total Duration & Size							**28866s**	**2022.69GB**

* RGB: 3840×2160@30fps H.265; Event: 1280×720 @ variable rate; LiDAR: Full area coverage

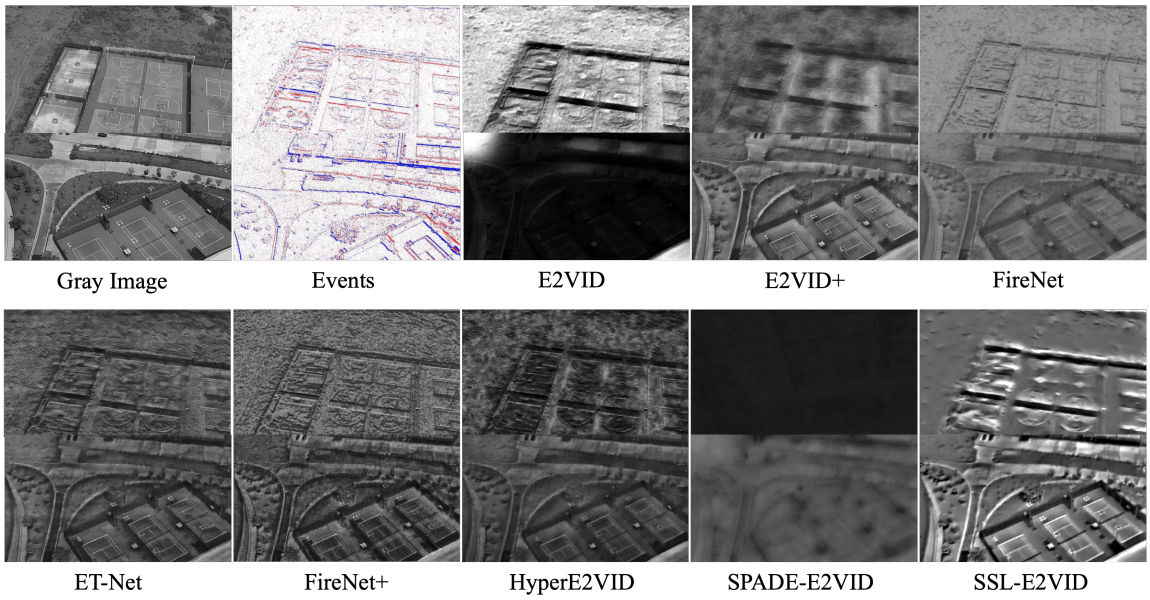

Figure 13: Video reconstruction with E2VID, E2VID+, FireNet, ET-Net, FireNet+, HyperE2VID, SPADE-E2VID, and SSL-E2VID.

A.7 Other Tasks to Explore

Figure 13 shows the performance of existing event-to-video reconstruction methods E2VID (Rebecq et al., 2019), E2VID+ (Stoffregen et al., 2020), FireNet (Scheerlinck et al., 2020), ET-Net (Weng et al., 2021), FireNet+ (Stoffregen et al., 2020), HyperE2VID (Ercan et al., 2024), SPADE-E2VID (Cadena et al., 2021), and SSL-E2VID (Paredes-Vallés & De Croon, 2021) when applied to our SkyEvents dataset.